Distinguishing spin pumping from spin rectification in lateral spin pumping device architectures based on doped organic semiconductors

Piotr Skalski,* Olga Zadvorna,* Deepak Venkateshvaran, and Henning Sirringhaus
Cavendish Laboratory, University of Cambridge, J.J. Thomson Ave, Cambridge CB3 0HE, United Kingdom
(Dated: February 1, 2022)

Over the last two decades organic spintronics has developed into a striving field with exciting reports of long spin diffusion lengths and spin relaxation times in organic semiconductors (OSCs). Easily processed and inexpensive, OSCs are considered a potential alternative to inorganic materials for use in spintronic applications. Spin currents have been detected in a wide range of materials, however, there is still uncertainty over the origin of the signals. Recently, we explored spin transport through an organic semiconductor with lateral spin injection and detection architectures, where the injected spin current is detected non-locally via spin-to-charge conversion in an inorganic detector. In this work we show that the widely-used control experiments like linear power dependence and inversion of the signal with the magnetic field are not sufficient evidence of spin transport and can lead to an incorrect interpretation of the signal. Here, we use in-plane angular dependent measurements to separate pure spin signal from parasitic effects arising from spin rectification (SREs). Apart from well established anisotropic magnetoresistance (AMR) and anomalous Hall effect (AHE), we observe another spurious effect originating in Py and having the same angular symmetry as the ISHE, which suggests it might be a self-induced ISHE.

I. INTRODUCTION

Organic semiconductors are a class of van der Waals bonded soft materials predominantly composed of light chemical elements such as carbon, hydrogen and sulphur. Owing to their composition, the spin orbit coupling within these materials is smaller compared to crystalline inorganic semiconductors, such as silicon or gallium arsenide. The reduced spin-orbit coupling in organic semiconductors in turn manifests itself through long carrier spin lifetimes, typically on the order of several microseconds [1],[2]. Such durations are long enough for the coherent manipulation of quantum spin information to be carried out and opens up new uses for organic semiconductors in spintronics. One drawback of the intrinsic nature of van der Waals bonding and the lack of consistent long-range order in organic semiconductors, however, is that their charge carrier mobilities tend to be comparatively low and typically on the order of 1 $\mathrm{cm^2V^{-1}s^{-1}}$. The immediate consequence of such low mobilities for spintronics is that the spin diffusion lengths within devices are expected to be small, as the spin diffusion length is computed using the relation $L_\mathrm{S} = \sqrt{D\tau_\mathrm{S}}$. Here L_S is the spin diffusion length, τ_S is the carrier spin lifetime and D is the diffusion constant linked to the carrier mobility μ with Einstein's relationship $D = \mu k_\mathrm{B}T/q$. It thus comes as no surprise that the reported values of the spin diffusion lengths in several undoped organic semiconductors (e.g. $\mathrm{Alq_3}$, P3HT, PPV and TIPS-Pentacene) were typically measured to be under 100 nm [3],[4],[5],[6],[7],[8],[9],[10]. It also becomes evident that the only way to boost the magnitude of the spin diffusion length beyond 100 nm in organic semiconductors is to amplify the diffusion constant D, for which purpose a new mechanism based on spin exchange transport was proposed [11],[12],[13].

The sub-100 nm spin diffusion lengths mentioned above were measured using devices known as vertical organic spin-valves. Vertical organic spin valves sandwich an organic semiconductor layer between two ferromagnetic thin film electrodes and show a switching behaviour in the electrically measured magnetoresistance of the trilayer stack in response to an applied magnetic field. Organic spin valves are easy to fabricate and their magnetoresistance measurements are relatively straightforward to interpret. However, the following three recently identified issues call into question the unambiguity of organic spin valve-based measurement techniques. First, it has been suggested that an alternative mechanism for the magnetoresistance switching signals in the organic trilayer stack stems from biaxial anisotropy and Tunnelling Anisotropic Magneto Resistance (TAMR) of the ferromagnetic electrode itself [14]. Second, there has never been an unambiguous demonstration of the Hanle effect within organic spin valves [15]. Third, a lack of scaling in the resistance-area products of some organic spin valve junctions casts light on the role pinholes play in a measured magnetoresistance signal [16]. Pinholes are understood to develop within the organic spin valve during device fabrication, when the top ferromagnetic electrode is deposited onto a soft organic sandwich layer.

The above challenges in unambiguously performing spin transport measurements within organic semiconductor spin valves call for improved techniques. In the recent past, we attempted to overcome some of the aforementioned challenges by using a new all-electrical device-based method known as lateral spin pumping (LSP) [17]. A schematic diagram of the lateral spin pumping device and the voltage measurement is shown in fig. 1. For spin current injection into the organic semiconductor a non-equilibrium spin current is generated by spin pumping

* These two authors contributed equally

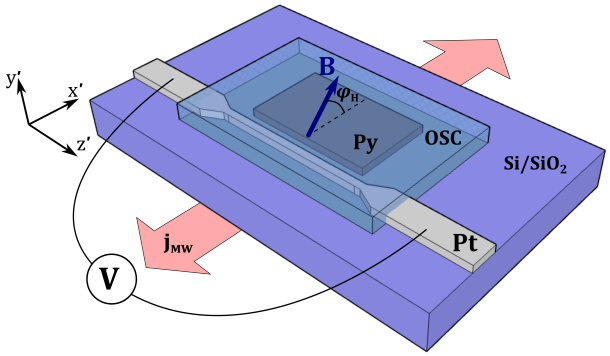

FIG. 1: A schematic diagram of the LSP sample architecture and the voltage measurement. An in-plane magnetic field **B** is applied at an angle φ_{H} to the direction of the microwave current $\mathbf{j}_{\mathrm{MW}}$. A voltage V is measured across the Pt stripe as the magnetic field is rotated in the sample plane.

using microwave excitation of ferromagnetic resonance within a thin film magnet in the device. The injected spin current is then assumed to propagate laterally through the organic semiconductor in contact with the thin film magnet. When the spin current arrives at a heavy metal stripe (platinum), which is positioned in proximity to the ferromagnetic spin injector but is only in direct contact with the organic semiconductor, it is converted into an electromotive force by the inverse spin Hall effect (ISHE). A measurable electromotive force is accepted evidence of spin transport within such a device. The device fabrication scheme incorporates the organic semiconductor in a final step thus ensuring no damage to the soft spin transport layer. The technique also overcame several associated intrinsic measurement difficulties presented by nonlocal spin valve devices that use organic semiconductors [17].

Lateral spin pumping is an extension of bilayer spin pumping that was first postulated in the late 1970s within non-magnet/ferromagnet stacks [18], where a spin current is generated in the non-magnet through the dissipation of angular momentum within a ferromagnet that it sits in contact with [19]. However, it wasn't until the mid 2000s that the first experimental attempt to validate the theory was made [20]. This demonstration made use of a permalloy/platinum bilayer where the spin current was excited within permalloy and detected within platinum using the inverse spin Hall effect. The technique inspired similar measurements on permalloy/non-magnet bilayers and was used to estimate the spin Hall angle of the non-magnetic spin detector [21]. In recent years however, the use of conductive ferromagnets such as permalloy within spin pumping devices has been discouraged, primarily due to a newly understood effect known as spin rectification. In spin rectification, a mixing signal between an rf generated current and the magnetoresistance in the conductive ferromagnet can yield a dc voltage component which can contribute to the signal and has similar symmetries as the signal generated by the inverse spin Hall effect [22].

In the past, lateral spin pumping using permalloy spin injectors was used to probe spin transport in a variety of materials including p-Si, [23] n-GaAs, [24] graphene, [25] n-Ge, [26] Cu, [27] and in a two-dimensional electron gas [28]. These studies were a basis for our own earlier work on lateral spin pumping into an organic semiconductor [17]. The aforementioned studies, however, did not investigate the potential contributions to the measured signal from spin rectification (SRE) which can accompany the use of conductive ferromagnets and arise from spin rectification [29],[30],[31],[32].

In this work, we extend our earlier study and demonstrate how contributions from spin rectification can be assessed within an organic lateral spin pumping device that uses conductive ferromagnetic injectors. We demonstrate the need for additional angular dependent measurements of the lateral spin pumping signal and identify various components to the measured 'spin signal'. In addition to angular dependent measurements on lateral spin pumping devices, we use various on-chip scaling approaches in both inorganic bilayers as well as devices which include an organic semiconductor, to systematically study how the components of spin rectification may be minimised in future experiments. Our study will be of interest to both the organic spintronics as well as the inorganic spintronics communities, as it highlights the need for greater scrutiny in the interpretation of such lateral spin pumping measurements.

II. THEORY

A. Ferromagnetic resonance

The dynamic behaviour of a ferromagnetic thin film can be modelled by the phenomenological Landau-Lifshitz-Gilbert equation [33] which describes the precession of the magnetisation $\boldsymbol{M}$ under the influence of a magnetic field $\vec{H}$

$$\frac{d\boldsymbol{M}}{dt} = -\gamma \boldsymbol{M} \times \vec{H} + \frac{\alpha}{M_{\mathrm{s}}} \boldsymbol{M} \times \frac{d\boldsymbol{M}}{dt}, \qquad (1)$$

where γ, α and M_{s} are the gyromagnetic ratio, Gilbert damping parameter and saturation magnetisation, respectively. The magnetic field $\boldsymbol{H}$ includes contributions from the external magnetic field as well as the demagnetisation fields.

To include the effect of the microwave magnetic field $he^{-i\omega t}$ oscillating at a frequency ω and analyse the in-plane angular dependence, we follow a similar procedure as in [32] and define a coordinate system (x, y, z) which rotates together with the magnetisation $\boldsymbol{M}$ aligned with the z axis, as shown in fig. 2a. The coordinates of the rotating frame (x, y, z) and the laboratory frame (x', y', z')

are related by a rotation matrix $R_y(\pi/2+\varphi_H)$ about the y axis, where φ_H is the in-plane angle between the magnetic field $\boldsymbol{H}$ and the direction of the microwave waveguide, which is the x' axis. Solving eq. 1 for the ac magnetisation $me^{-i\omega t}$ yields the dynamic susceptibility tensor χ which relates the oscillating magnetisation $\boldsymbol{m}$ and magnetic field $\boldsymbol{h}$ in the following way:

$$\boldsymbol{m} = \boldsymbol{R_y}(\pi/2+\varphi_H)\,\boldsymbol{\chi}\,\boldsymbol{R_y}(-\pi/2-\varphi_H), \tag{2}$$

$$\boldsymbol{\chi} = \begin{pmatrix} A_{xx} & iA_{xy} & 0 \\ iA_{xy} & A_{yy} & 0 \\ 0 & 0 & 0 \end{pmatrix}, \tag{3}$$

$$A_{xy} = \frac{-4\pi M_s}{\alpha(2H_0+4\pi M_s)}, \tag{4a}$$

$$A_{xx} = -\frac{A_{xy}\gamma(H_0+4\pi M_s)}{\omega}, \tag{4b}$$

$$A_{yy} = -\frac{A_{xy}\gamma H_0}{\omega}. \tag{4c}$$

The behaviour of ferromagnetic resonance (FMR) is captured by L and D which define the symmetric and antisymmetric lineshape components:

$$L = \frac{\Delta H^2}{4(H_0-H_r)^2+\Delta H^2}, \tag{5a}$$

$$D = \frac{2\Delta H(H_0-H_r)}{4(H_0-H_r)^2+\Delta H^2}. \tag{5b}$$

In the above equations H_r and ΔH are the resonant field value and the resonance linewidth (full-width at half-maximum).

The following sections consider generation of voltage during FMR as a result of spin pumping and spin rectification. In order to calculate the magnitude of the induced voltages, one has to know the resistance values of the different layers that constitute the electrical circuit. Unlike bilayer or trilayer structures, where the layers in an electrical circuit could simply be represented by two or three resistors connected in parallel, an LSP circuit diagram is not straightforward. The OSC layer cannot be represented by a single resistor due to the complex geometry of the device architecture. An approximation of the electrical circuit is shown in figure 2 (b). DC sources represent ISHE in the Pt detector and the SREs originating in the Py layer.

In order to simplify the analysis, we consider instead a Pt/Py vertical bilayer structure where the dependence of generated voltages on the conductivity and thickness of Pt and Py layers can be computed exactly. While this model cannot be used directly with LSP samples, the derivation of in-plane angular dependence is expected to be valid in both vertical and lateral geometries. We can therefore use it to extract different voltage components in LSP experiments based on their angular symmetries.

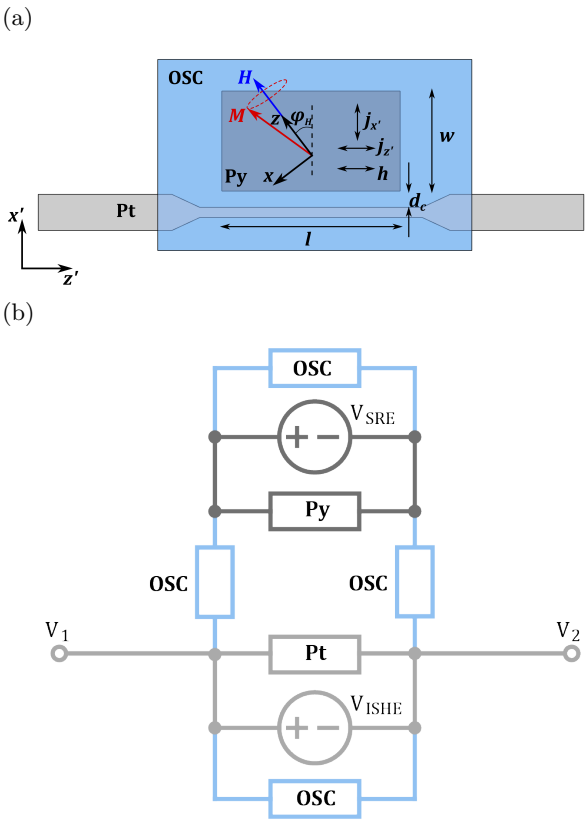

FIG. 2: (a) a two-dimensional, top-view diagram of the LSP sample showing directions of the external field $\boldsymbol{H}$, magnetisation $\boldsymbol{M}$ as well as induced microwave currents $\boldsymbol{j_{x'}}$, $\boldsymbol{j_{z'}}$ and magnetic field $\boldsymbol{h}$ (b) an approximation of the LSP electrical circuit with V_{ISHE} generated across the Pt stripe and spin rectification voltage V_{SRE} generated across the Py magnet. A voltage is measured between V_1 and V_2.

B. Spin pumping and inverse spin-Hall effect

Let's consider a Py/Pt bilayer under the FMR condition. Magnetisation dynamics causes spin angular momentum transfer from Py to Pt in the form of a spin current. The spin current is converted into a charge current via ISHE

$$\boldsymbol{j_c} = \frac{2e\theta_{SHE}}{\hbar}\hat{y}\times\boldsymbol{j_s}, \tag{6}$$

where $\boldsymbol{j_s}$ is the spin current averaged over the Pt thickness and takes the form [34]

$$\boldsymbol{j_s} = \frac{\hbar\lambda_{Pt}g_{eff}^{\uparrow\downarrow}}{4\pi M_0^2 d_{Pt}}\tanh\left(\frac{d_{Pt}}{2\lambda_{Pt}}\right)Re\left\{\boldsymbol{M}\times\frac{d\boldsymbol{M}}{dt}\right\}. \tag{7}$$

Here, M_0 is the magnitude of equilibrium magnetisation, λ_{Pt} is the spin diffusion length in Pt, d_{Pt} is the thickness of the Pt film and $g_{eff}^{\uparrow\downarrow}$ is the real part of the effective spin mixing conductance. By substituting the solution

to eq. 2, time averaged and scaled by the resistance of the bilayer, we can obtain the final form of the DC component of the ISHE voltage

$$V_{\mathrm{ISHE}}^{\mathrm{DC}} = -f_{\mathrm{Pt}} K A_{\mathrm{xy}} A_{\mathrm{xx}} h^2 \omega \cos^3\varphi_{\mathrm{H}} \cdot \mathrm{L}, \tag{8}$$

where $K = we\theta_{\mathrm{SHE}} g_{\mathrm{eff}}^{\uparrow\downarrow} \lambda_{\mathrm{Pt}} \tanh(d_{\mathrm{Pt}}/2\lambda_{\mathrm{Pt}})/64\pi^3 M_{\mathrm{s}}^2$ and $f_{\mathrm{Pt}} = 1/(d_{\mathrm{Pt}}\sigma_{\mathrm{Pt}} + d_{\mathrm{Py}}\sigma_{\mathrm{Py}})$, with d_{Pt}, d_{Py} and σ_{Pt}, σ_{Py} being the thickness and conductivity values for Pt and Py layers, respectively.

C. Spin rectification effects

To analyse the angular dependence of the SRE, we start by considering the generalised Ohm's law [35] which couples together the current density $\boldsymbol{J}$, magnetisation $\boldsymbol{M}$, electric field $\boldsymbol{E}$ and magnetic field $\boldsymbol{H}$ inside the ferromagnet

$$\boldsymbol{J} = \sigma\boldsymbol{E} - \frac{\sigma\Delta\rho}{M^2}(\boldsymbol{J}\cdot\boldsymbol{M})\boldsymbol{M} + \sigma R_{\mathrm{H}}(\boldsymbol{J}\times\boldsymbol{H}) + \sigma R_{\mathrm{AHE}}(\boldsymbol{J}\times\boldsymbol{M}). \tag{9}$$

The terms in this equation represent the usual Ohmic contribution, anisotropic magnetoresistance (AMR), standard Hall effect and anomalous Hall effect (AHE) contributions, respectively. σ, $\Delta\rho$, R_{H} and R_{AHE} are the conductivity, change in resistivity due to AMR, ordinary and anomalous Hall coefficients. Time-averaging the above expression yields a DC current

$$\begin{aligned}\boldsymbol{J}_{\mathrm{SRE}} = &-\frac{\sigma\Delta\rho}{M^2}\left(\langle\boldsymbol{j}\times\boldsymbol{m}\rangle\times\boldsymbol{M} + \langle\boldsymbol{j}\cdot\boldsymbol{m}\rangle\boldsymbol{M}\right)\\ &+ \sigma R_{\mathrm{H}}\langle\boldsymbol{j}\times\boldsymbol{h}\rangle + \sigma R_{\mathrm{AHE}}\langle\boldsymbol{j}\times\boldsymbol{m}\rangle,\end{aligned} \tag{10}$$

where $\boldsymbol{j}$, $\boldsymbol{h}$ and $\boldsymbol{m}$ are the ac components of the microwave-induced current, magnetic field and magnetisation. These three quantities oscillate at the same frequency ω but with different phases. Specifically, $\boldsymbol{j}$ and $\boldsymbol{h}$ oscillate with a relative phase Φ which is usually referred to as the electromagnetic phase difference. The usual Hall contribution being independent of magnetisation results in a constant offset, therefore will be ignored in further analysis.

In our geometry the microwave current $\boldsymbol{j}$ flows mostly in the x' direction. However, due to the complexity of transmission line-to-sample coupling and possible sample misalignment on the coplanar waveguide (CPW), we allow for the current to have two in-plane components $\boldsymbol{j}_{\mathrm{x}'}$ and $\boldsymbol{j}_{\mathrm{z}'}$. Using the solution to eq. 2 we obtain the final expression for the SRE voltage signal along the measurement direction z':

$$V_{\mathrm{SRE}} = A_{\mathrm{L}} \cdot \mathrm{L} + A_{\mathrm{D}} \cdot \mathrm{D}, \tag{11a}$$

$$\begin{aligned}A_{\mathrm{L}} = &sin\Phi \cdot (V_{\mathrm{AMR}}^{\mathrm{x}} \cos\varphi_{\mathrm{H}} \cos 2\varphi_{\mathrm{H}} - V_{\mathrm{AMR}}^{\mathrm{z}} \cos\varphi_{\mathrm{H}} \sin 2\varphi_{\mathrm{H}})\\ &-\cos\Phi \cdot V_{\mathrm{AHE}} \cos\varphi_{\mathrm{H}},\end{aligned} \tag{11b}$$

$$\begin{aligned}A_{\mathrm{D}} = &-cos\Phi \cdot (V_{\mathrm{AMR}}^{\mathrm{x}} \cos\varphi_{\mathrm{H}} \cos 2\varphi_{\mathrm{H}} - V_{\mathrm{AMR}}^{\mathrm{z}} \cos\varphi_{\mathrm{H}} \sin 2\varphi_{\mathrm{H}})\\ &-\sin\Phi \cdot V_{\mathrm{AHE}} \cos\varphi_{\mathrm{H}},\end{aligned} \tag{11c}$$

where L and D are the symmetric and antisymmetric lineshapes defined in eqs. 5.

The voltage contributions due to AMR from microwave currents $\boldsymbol{j}_{\mathrm{x}'}$ and $\boldsymbol{j}_{\mathrm{z}'}$, and due to AHE are:

$$V_{\mathrm{AMR}}^{\mathrm{x}} = f_{\mathrm{Py}} A_{\mathrm{xx}} h j_{\mathrm{x}'} \Delta\rho w/8\pi M_{\mathrm{s}}, \tag{12a}$$

$$V_{\mathrm{AMR}}^{\mathrm{z}} = f_{\mathrm{Py}} A_{\mathrm{xx}} h j_{\mathrm{z}'} \Delta\rho w/8\pi M_{\mathrm{s}}, \tag{12b}$$

$$V_{\mathrm{AMR}}^{\mathrm{x}} = f_{\mathrm{Py}} A_{\mathrm{xy}} R_{\mathrm{AHE}} j_{\mathrm{x}'} hw/2. \tag{12c}$$

The factor $f_{\mathrm{Py}} = d_{\mathrm{Py}}\sigma_{\mathrm{Py}}/(d_{\mathrm{Py}}\sigma_{\mathrm{Py}} + d_{\mathrm{Pt}}\sigma_{\mathrm{Pt}})$ incorporates shorting of the SRE voltage contributions by the Pt layer.

One can see that the lineshape of SREs is strongly dependent on the electromagnetic phase Φ. It is a material and frequency dependent parameter related to the losses in the system – an electromagnetic wave propagating through an absorptive medium has a complex wave vector, whose imaginary contribution creates a phase shift between electric and magnetic fields. It is difficult to compute Φ in a system such as ours with a complex coupling between the CPW and a metallic sample, and therefore it is treated as one of the fitting parameters. Previous work [31] showed that it can change significantly within a small range of microwave frequencies and between different samples.

In general, each SRE component can create both a symmetric and an antisymmetric voltage signal, which makes it impossible to distinguish ISHE from SRE based solely on the lineshape symmetry. However, they can be separated based on the dependence on the in-plane angle φ_{H}. Figure 3 shows the expected angular dependence profiles for each voltage component. This forms the basis of our analysis in this paper - after extracting A_{L} and A_{D} values from a magnetic field sweep at each angle, we then

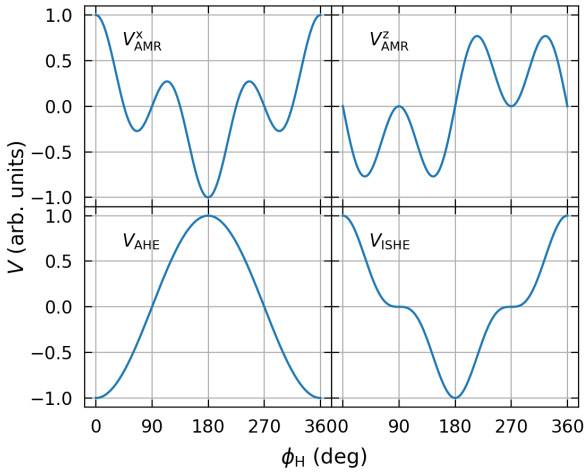

FIG. 3: Modelled in-plane angular dependence of the ISHE signal and the three SRE contributions: $\mathrm{AMR}^{\mathrm{x}}$, $\mathrm{AMR}^{\mathrm{z}}$ and AHE.

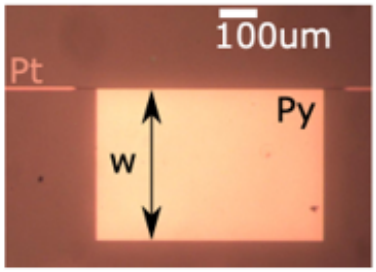

FIG. 4: A micrograph of the device showing the central region before deposition of the OSC.

fit eqs. 8 and 11 to extract the four contributions: V^{x}_{AMR}, V^{z}_{AMR}, V_{AHE} and V_{ISHE}. This analysis applies directly to a bilayer system. In the LSP geometry the prefactors in eq. 12 containing the dependence on the geometric dimensions and the conductivity of the different materials would need to be adjusted, but the angular dependence analysis remains valid.

III. METHODS

A. Device fabrication

All of the devices were fabricated on 3 mm x 5 mm Si/SiO_2 (300 nm) substrates. The lateral spin pumping devices were produced with the multistep ebeam lithography method used in reference [17]. Firstly, a 10 nm thick, 1 μm wide Pt stripe was defined with electron beam lithography and subsequently deposited using magnetron sputtering at 1 x 10^{-6} mbar base pressure and 5 x 10^{-4} partial Ar gas pressure at 4.5 Å/s rate. Secondly, a 600 μm x 400 μm x 25 nm Py injector was evaporated using an electron beam at 2 Å/s under 2 x 10^{-7} mbar pressure. It was aligned parallel to the Pt stripe at a distance of 200 nm away from it by a second electron beam lithography step. Figure 4 shows a microscope image of the active area of the LSP device at this stage in the fabrication process. Thirdly, the conjugated polymer poly[2,5-bis(3-tetradecylthiophen-2-yl)thieno[3,2-b]thiophene], also called PBTTT, was spin coated on top from a 10 g/l DCB solution at 5000 rpm in nitrogen atmosphere. The film was annealed at 180°C for 20 min and slowly cooled back to room temperature to form the terraced phase. Finally, the devices were placed in 1 g/l F4TCNQ:ACN solution to dope the OSC. They were then annealed at 80°C for 20 min to allow the dopant to diffuse into the film. The estimated conductivity achieved for these films was around 100 Scm^{-1}. The doped OSC film was patterned into a box covering the Py injector, the channel, and the Pt stripe by scratching the excess with a cocktail stick. The stripe was attached to wider, 10 μm Pt pads which were used to contact the device with silver dag.

To fabricate the bilayer devices we deposited the bottom contact (Au or Pt) through a 2 mm x 4 mm shadow mask. Au was thermally evaporated at 1 x 10^{-6} mbar base pressure while Pt was sputtered under the same conditions as the LSP devices above. Py was subsequently deposited on top of the contact through a 2 mm x 0.5 mm shadow mask using e-beam evaporation under identical conditions to the LSP devices.

B. Measurement setup

All of the device voltages were measured using a CPW based spin pumping setup with an in-plane magnetic field rotation. A magnetic field was applied in the plane of the device at different angles φ_H to magnetise the FM film. An in-plane 4 GHz microwave field was applied using a CPW with a 700 μm wide central conductor. The devices were contacted with Ag paste and placed face down on the CPW to maximise power absorption. To accurately measure the ferromagnetic absorption, a lock-in measurement technique was employed with magnetic field modulation at 20 Hz and modulation amplitude approximately 0.1 mT. To this end, one side of the CPW was connected to an Stanford Research Systems SR860 DSP lock-in amplifier through a rectifying diode. The device voltage was measured using a KEITHLEY 2182A Nanovoltmeter (see appendix B for a schematic diagram of the electrical connections). The measurements were performed at 5° steps as the magnetic field was rotated in-plane from φ_H=0° to 360°.

C. Data collection and analysis

At each magnetic field angle φ_H both the device voltage and microwave absorption were measured as a function of the magnetic field H to capture the FMR. Each voltage scan was then fitted numerically with a combination of lineshapes in eq. 5 to obtain best fit values of V_L and V_D, corresponding to the magnitudes of the symmetric and antisymmetric Lorentzian lineshapes. The absorption scans were fitted with derivatives of the two lineshapes to extract P_L and P_D amplitudes, which allowed us to quantify the absorbed power as P^2_L. Next, each voltage component was plotted as a function of the angle φ_H and a second numerical fitting step was performed where V_L and V_D angular dependencies were fitted simultaneously with a combination of eqs. 8 and 11. This allowed us to extract the best fit values for Φ, V^{x}_{AMR}, V^{z}_{AMR}, V_{AHE} and V_{ISHE}.

IV. LATERAL SPIN PUMPING

We produced a LSP device with F4TCNQ-doped PBTTT film and 200 nm channel length. In line with previous experiments on spin pumping, we measured the

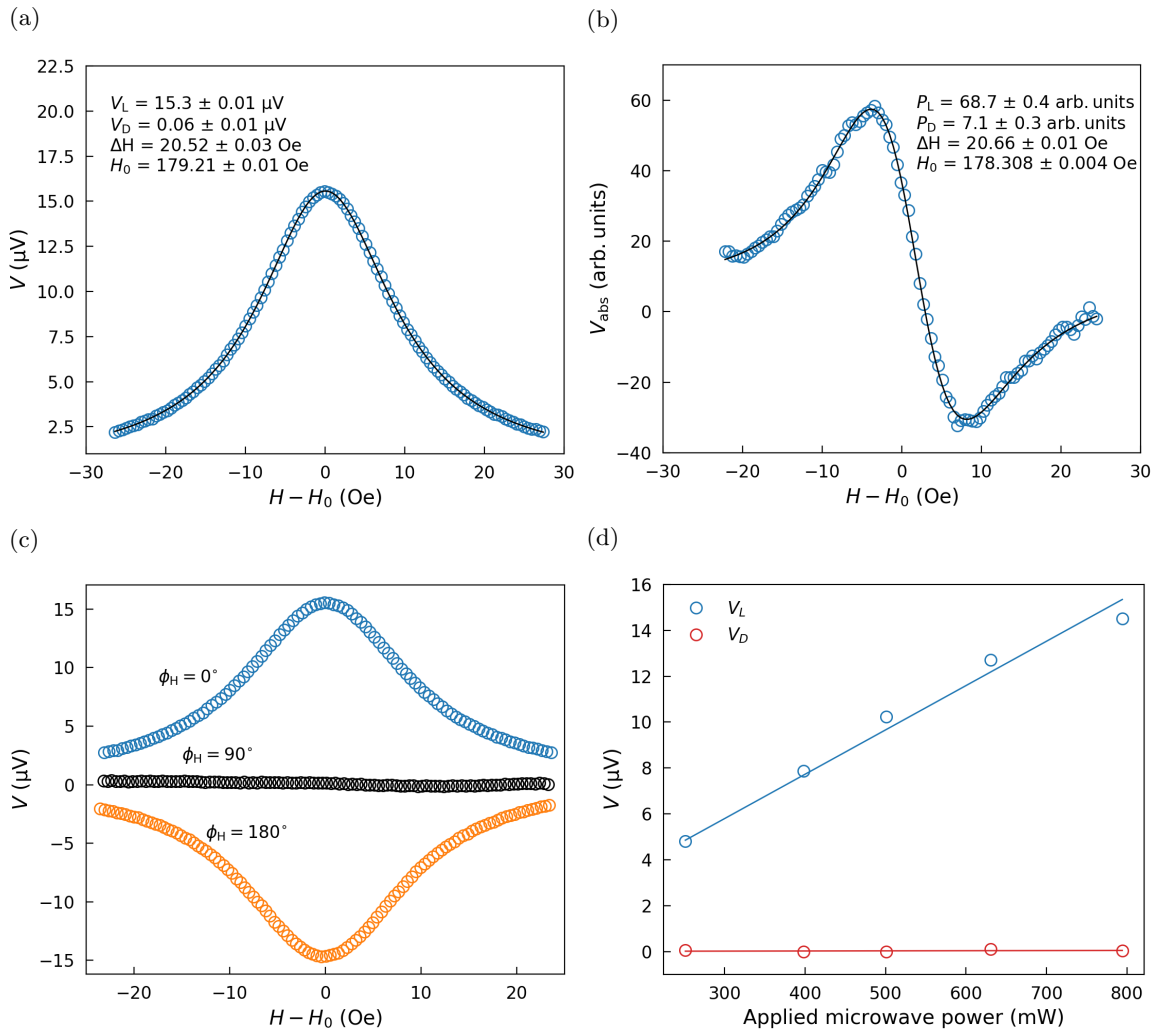

FIG. 5: LSP device with F4TCNQ-doped PBTTT and a 200 nm channel length between the Py injector and Pt detector. (a) Voltage signal measured across the device and (b) the FMR absorption amplitude from the lock-in amplifier measured at $\varphi_H = 0^\circ$ as a function of the applied magnetic field H. The P_L and P_D represent power absorption components from the symmetric and antisymmetric lineshapes obtained from numerical fits of the absorption signal V_{abs} to the derivatives of the two lineshapes. (c) Voltage signal measured at three orientations of the magnetic field: $\varphi_H = 0^\circ$, 90° and 180°. (d) Power dependence of the voltage signal at $\varphi_H = 0^\circ$.

device voltage as a function of magnetic field at three critical in-plane angles: $\varphi_H = 0^\circ$, 90° and 180°, and produced a microwave power dependence plot. Our results are shown in figs. 5 and 6. The voltage profile in fig. 5(a) can be well fitted with a combination of a symmetric and an antisymmetric Lorentzian lineshapes, and its peak aligns with the position of the FMR absorption (fig. 5(b)) at 179 Oe. In literature, the symmetric Lorentzian contribution has been attributed to the ISHE, while the antisymmetric Lorentzian contribution has simply been identified as coming from the AHE. Moreover, from fig. 5(c) it can be seen that the voltage signal disappears at $\varphi_H = 0^\circ$ and has an opposite sign at $\varphi_H = 180^\circ$ - this symmetry argument, while being in agreement with ISHE, has often been used to confirm the origin of the spin pumping voltage.

We argue, however, based on the angular dependence analysis of SREs that this simple symmetry argument is not sufficient to identify the origin of the voltage signal. Firstly, according to eq. 11, rectified AHE as well as AMR can contribute to both symmetric and antisymmetric parts of the voltage signal. Only in certain special case can the symmetric part be free from spurious effects: either $\Phi = 0^\circ$ and $V_{AHE} = 0$, or $\Phi = 90^\circ$ and $V^x_{AMR} = V^z_{AMR} = 0$. Secondly, as shown in fig. 3, both AHE and AMR^x reduce to zero at $\varphi_H = 90^\circ$ and have an opposite sign at $\varphi_H = 180^\circ$, therefore the results from fig. 5(c) are consistent not only with ISHE but also with the expected AHE and AMR^x symmetries. Moreover, the linear power dependence of the voltage signal, fig. 5(d), has been used in literature to further support the sym-

metry argument. The SREs, however, are also expected to have a linear power dependence. Both AHE and AMR can be expressed as a product of $\boldsymbol{m}$ with either $\boldsymbol{h}$ or $\boldsymbol{j}$, each of these three quantities has a square root dependence on the microwave power. Therefore, the end effect is linearly proportional to the absorbed power.

Nevertheless, the SRE and ISHE can be distinguished from one another by measuring a full in-plane angular dependence, since each of them has a distinct φ_{H} dependence as pictured in fig. 3. Therefore, we performed a full in-plane angular dependence measurement on the same device. Results and the corresponding numerical fits are plotted in fig. 6. Various contributions to the spin pumping voltage were extracted with the largest one being $V^{\mathrm{x}}_{\mathrm{AMR}} = 12.6\ \mu\mathrm{V}$ followed by $V_{\mathrm{ISHE}} = 2.5\ \mu\mathrm{V}$. This finding contradicts the earlier assumption that the SP voltage measured in an LSP architecture originates purely from the ISHE and signifies the importance of the in-plane angular dependence analysis. It also shows that the dominant spurious effect is AMR rather than AHE, which is consistent with similar recent experiments that make use of conductive ferromagnets as spin injectors [29],[30],[31],[32].

Considering that the extracted V_{ISHE} component was a small contribution to the overall voltage signal, we performed further control experiments to confirm or rule out the existence of ISHE in spin pumping device architectures.

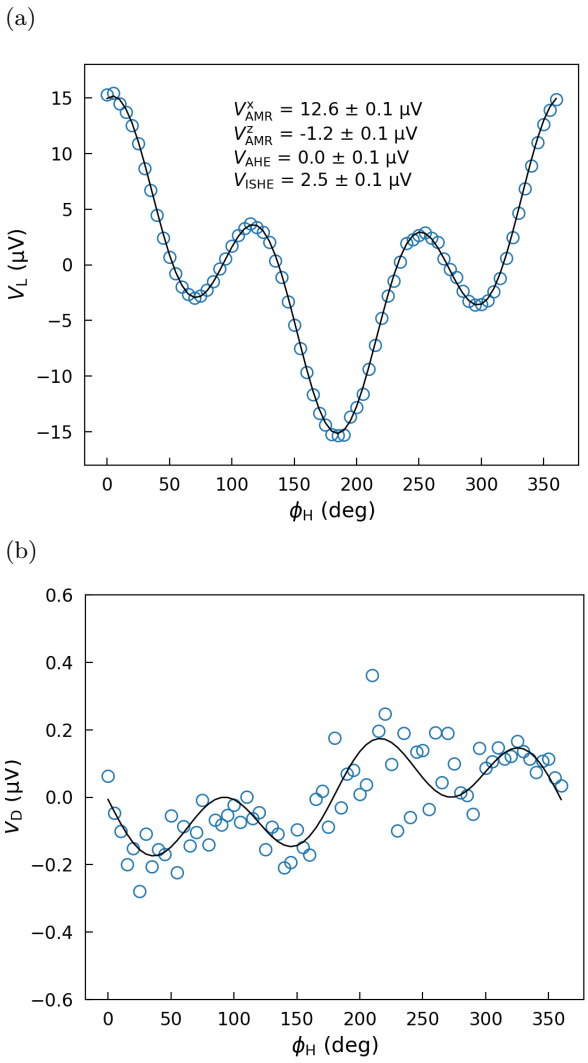

FIG. 6: LSP device with F4TCNQ-doped PBTTT and a 200 nm channel length between Py injector and Pt detector. In-plane angular dependence of (a) symmetric and (b) antisymmetric voltage components, respectively. Solid lines show numerical fits.

A. Discontinuous Pt electrode experiment

The LSP device architecture was modified to include a second Pt electrode on the opposite side of the Py injector, as shown in fig. 7 (inset). This additional Pt electrode was intentionally discontinuous and only extended 3 μm on either side next to the 600 μm long Py injector. With this architecture, in theory, the standard Pt electrode would convert the spin current into a charge current via the ISHE. It would also pick up any spurious voltage generated by the Py injector. Since the Pt stripe is missing on the other side, the discontinuous electrode, very little ISHE voltage is expected to be observed across this electrode, however any spurious voltage from Py would still be measurable.

Putting both Pt electrodes on the same device allowed us to control for device-to-device variations in Py/OSC qualities and hence spin injection/transport properties. Furthermore, it ensured that the contributions to the device resistance from the organic semiconductor and the Py injector were the same, making the resistance across both electrodes comparable.

The resulting voltage contributions measured across each electrode separately are summarised in fig. 7. Since the device had to be remounted between the two measurements, we normalised the voltages across the two electrodes by power absorbed extracted from the FMR absorption curves. It should be noted that normalising for absorption only takes into account the quality of the bulk of the Py electrode. The interface is not necessarily the same between the samples and is a very significant factor in spin pumping. Having the two devices on the same chip, reduces this uncertainty.

The dominant contribution to the signal for both electrodes is the AMR voltage from the Py ferromagnet as in the previous LSP device. The relative weights of the $\mathrm{AMR}^{\mathrm{x}}$ and $\mathrm{AMR}^{\mathrm{z}}$ contributions depend on the exact orientation of the device with $\mathrm{AMR}^{\mathrm{z}}$ only appearing if the device is not strictly perpendicular to the microwave current. Opposite signs of $\mathrm{AMR}^{\mathrm{z}}$ of the two electrodes mean that the device was tilted in opposite directions between the two measurements. The V_{ISHE} component of around 2.5 μV was measured across the standard Pt electrode,

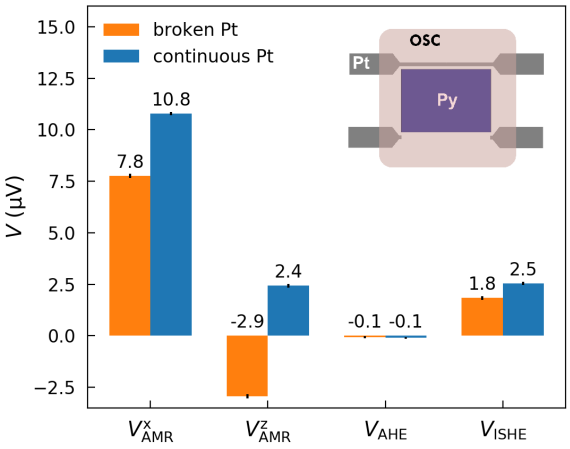

FIG. 7: Discontinuous platinum electrode experiment: comparison of the in-plane angular dependence voltage components for a LSP device with integrated continuous and discontinuous Pt electrodes on both sides of the Py injector (see inset).

identical to the LSP device in the previous section. Interestingly, a comparable magnitude of V_{ISHE} was also picked up by the discontinuous Pt electrode, which was not expected. Given that this electrode cannot create any ISHE, the voltage likely originates in the Py film - we have called it *spurious* ISHE. It is possible that the ferromagnet produces a self-induced ISHE voltage, previously reported in literature [36], [37], which would have the same $\cos^3\phi_{\mathrm{H}}$ angular dependence as the ISHE in Pt. To further investigate the ways to separate this spurious contribution from the spin pumping signal we have performed spin pumping measurements in bilayer systems, which are discussed in the next section.

Our findings highlight a further limitation of the LSP architecture used with conductive spin transport layers. Although the lateral architecture does not suffer from pinholes, which increase the coupling between the FM electrode and the detector electrode thus increasing the SREs weight in the SP voltage, the spurious voltages can still be dominant in a LSP device. Using a conductive material as a transport layer together with a conductive FM will inevitably lead to mixing of the pure ISHE signal and ISHE generated in the FM. To avoid this, it is necessary to minimize SREs and/or use a material that exhibits efficient spin transport, but is not electrically conducting. Some promising candidates include organic-based magnet $V(TCNE)_x$ (with $x \approx 2$) [38],[39] or inorganic magnetic oxides such as YIG [40].

V. BILAYER SPIN PUMPING

Motivated to explore the ISHE signal further, we have fabricated vertical bilayer spin pumping heterostructures

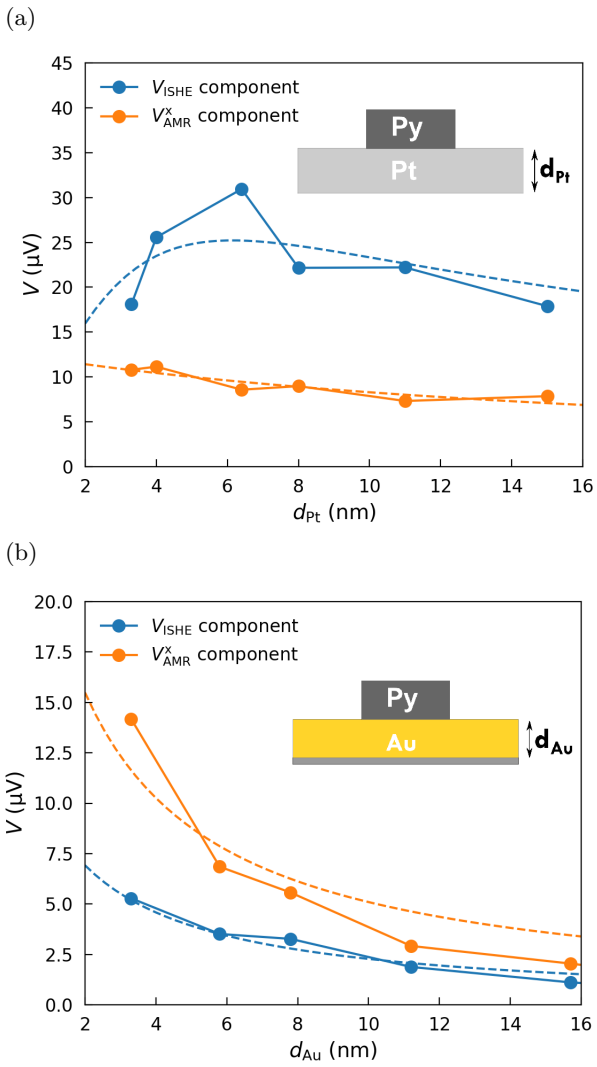

FIG. 8: V_{ISHE} and $V^{\mathrm{x}}_{\mathrm{AMR}}$ voltage contributions in Pt/Py (a) and Au/Py (b) bilayers as the non-magnet thickness was varied. Dotted lines show theoretical fits to the data. Each data point represents a single sample and the errors of extracting the different voltage components from numerical fits are below 100nV.

where the Py layer is deposited directly on top of the non-magnetic layer, either Pt or Au. By measuring Pt/Py and Au/Py bilayers, we can separate the contribution from spurious ISHE generated in Py and compare it with ISHE in Pt. Measurements of the thickness dependence of each layer can provide further distinguishing characteristics. Using thin films of Au, which has a smaller spin-Hall angle compared to Pt, allows us to reduce the contribution from spin pumping into Au and attribute the voltage signal to SRE and the spurious ISHE in Py. The idea is similar to the discontinuous Pt electrode experiment, however, unlike the LSP architecture, bilayers allow for a direct contact between the non-magnet and the ferromagnet which provides a strong spin pumping ef-

ficiency in NM/FM structures. Moreover, it is relatively straightforward to account for the conductivity and electrical shunting of various layers in the bilayer architecture.

Figure 8 shows non-magnetic layer thickness dependence of the V^{x}_{AMR} and V_{ISHE} voltage components (the two dominant contributions) with the thickness of Py being constant at 25 nm. It can be seen from fig. 8(a) that the V_{ISHE} component in Pt/Py bilayer has a typical non-monotonic thickness dependence in accordance with theoretical prediction for ISHE (eq. 8). Initially, it increases as $\tanh(d_{Pt}/2\lambda_{Pt})$ because more spin current is converted to charge current. It then saturates and starts decreasing on a larger length scale due to shunting of the signal by the conductance of the Pt layer as the thickness is increased. Numerical fit of eq. 8, shown by the blue, dashed line, was obtained by keeping the functional form of thickness-dependent terms while pulling the remaining factors into one free parameter, giving a new scaling equation of the form $V_{ISHE} = A \cdot \tanh(d_{Pt}/2\lambda_{Pt}) / (d_{Py}\sigma_{Pt} + d_{Py}\sigma_{Py})$. We used fixed conductivity values of $\sigma_{Py} = 1 \times 10^6$ Scm^{-1} and $\sigma_{Pt} = 1.3 \times 10^6$ Scm^{-1} measured using reference samples with the van der Pauw method, while A and λ_{Pt} were treated as the fitting parameters. The best fit value obtained for the spin diffusion length in Pt was $\lambda_{Pt} = 1.9$ nm which agrees with literature values [41],[42],[43]. This provides strong evidence that the dominant signal in Pt/Py devices can certainly be attributed to the ISHE in Pt. We stress that apart from the DC component of the ISHE measured in this experiment there also exists an AC component, however, it was disregarded in our experiments since it occurs in the gigahertz frequency range.

On the other hand, the V_{ISHE} component in Au/Py bilayer, shown in fig. 8(b), has a significantly different profile. It is over six times smaller compared to Pt/Py devices and decreases monotonically. Given that $\lambda_{Au} \approx 32$ nm [44], we would expect the ISHE in Au to show an initial increase over the range of thickness values probed in our experiment. Instead, the data can be modelled well with a thickness dependence expected for a signal originating in the Py layer. Both the orange and blue dashed lines (as well as the orange dashed line from fig. 8(a)) represent numerical fits of eq. 12. It was obtained from the thickness dependent terms captured in the factor $f_{Py} = d_{Py}\sigma_{Py} / (d_{Py}\sigma_{Py} + d_{Au}\sigma_{Au})$, while the remaining terms were collected in one fitting parameter. We used $\sigma_{Au} = 1.3 \times 10^7$ Scm^{-1} together with the conductivity value for Py as before. Therefore, we conclude that the V_{ISHE} component in this case is caused by the spurious ISHE from Py observed earlier in the discontinuous Pt electrode experiment.

Further evidence distinguishing spurious ISHE in Py from the ISHE in Pt caused by spin pumping can be obtained by varying the thickness of the Py film. Figure 9 shows the results of an experiment where the thickness of Pt and Au was kept constant at 7 nm and 5 nm respectively, while the thickness of Py was varied between 5 nm – 35 nm. For thicker Py films, the thickness dependence of the observed voltage components is captured by the factors f_{Pt} and f_{Py} in eqs. 8 and 12. The magnitude of SRE is expected to increase with d_{Py} and saturate at higher values, while the ISHE magnitude should decrease as the resistance of the shunting Py layer decreases. For thin Py films, modelling becomes more complicated since the Gilbert damping constant α increases rapidly with decreasing d_{Py} [45],[19], which leads to a decrease in both ISHE and SRE voltages. Furthermore, the equilibrium magnetisation M_0 for ultra-thin Py films reduces, which leads to a further drop in voltage. Dashed lines in fig. 9 show numerical fits, which include the explicit modelling

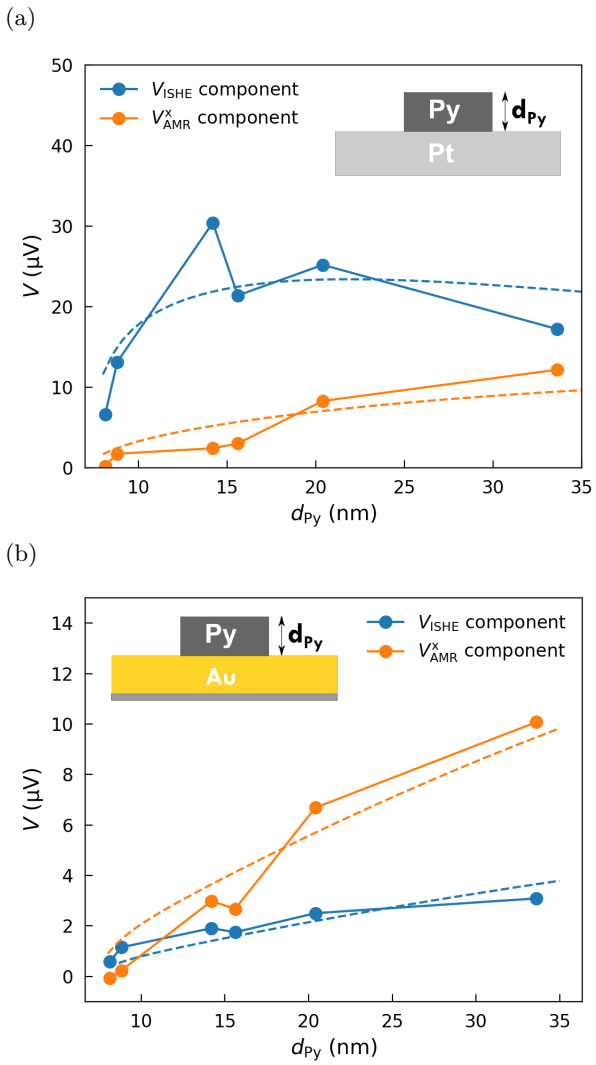

FIG. 9: V_{ISHE} and V^{x}_{AMR} voltage contributions in Pt/Py (a) and Au/Py (b) bilayers as the Py thickness was varied. Dotted lines show theoretical fits to the data. Each data point represents a single sample and the errors of extracting the different voltage components from numerical fits are below 100nV.

of α and M_0 (more details in the appendix A). While the V_{ISHE} component in fig. 9(a) was fitted with eq. 8 which describes ISHE from spin pumping, both $V^{\mathrm{x}}_{\mathrm{AMR}}$ components as well as the V_{ISHE} component in fig. 9(b) were best fitted with eq. 12, suitable for SRE. This is consistent with the previous observation and gives further support for the claim that the spurious ISHE measured in the broken Pt experiment originates in the Py layer.

VI. CONCLUSIONS

The experiments shown in this paper demonstrate that spin rectification effects due to AMR and AHE are an important source of spurious voltages in lateral as well as vertical spin pumping devices with a conductive ferromagnet and need to be considered when interpreting the voltage signals generated. Simple checks for symmetries such as comparing measurements upon inversion of the magnetic field are insufficient to prove the observation of a genuine ISHE signal. However, it is possible to separate SREs from ISHE through a full in-plane angular dependence. Our measurements here suggest that the majority of the voltage signal observed in our previous LSP study on organic semiconductors [17] should be interpreted as a rectified AMR signal rather than an ISHE signal. Even a small signal component that has the same angular symmetry as expected from a genuine ISHE signal that was detected both in LSP samples as well as in vertical bilayer systems may not be a genuine ISHE signal. Through careful control experiments we showed that it cannot be attributed to ISHE in Pt, but could rather be originating in the Py layer. Our results emphasise that analysing spin pumping voltages is more complex than previously assumed due to the existence of spin rectification effects and spurious ISHE voltage from the Py layer. As well as lateral architectures used in this paper, the findings will need to be considered in other architectures such as trilayers with organic semiconductors [46]. Our results point to a number of experimental design requirements for conducting successful spin pumping experiments with organic systems. These include: minimizing SRE through (a) careful optimisation of the thickness of the ferromagnet, or (b) the choice of a non-conducting ferromagnet such as YIG or organic ferromagnets like $\mathrm{V(TCNE)_x}$ (with $\mathrm{x} \approx 2$), and/or (c) minimizing the conductivity of the spin transport layer.

VII. ACKNOWLEDGEMENTS

The authors gratefully acknowledge funding from the European Research Council (ERC) through a Synergy Grant (Grant Agreement ID: 610115). D. Venkateshvaran acknowledges the Royal Society for funding in the form of a Royal Society University Research Fellowship (Royal Society Reference No. URF\R1\201590). The authors express their thanks to Dr Radoslav Chakalov, Mr Roger Beadle and Mr Tom Sharp for technical support.

Appendix A

In order to obtain more accurate numerical fits of the Py thickness dependence experiments performed on vertical Pt/Py and Au/Py bilayers, the behaviour of the Gilbert damping parameter α has to be modelled. For thin ferromagnetic films it strongly depends on thickness, which influences both the spin pumping and spin rectification voltages through the components of the susceptibility tensor χ (eq. 4 in the main text). The Gilbert damping parameter can be written as [19]

$$\alpha = \alpha_0 + \frac{\gamma \hbar g_{\mathrm{eff}}^{\uparrow\downarrow}}{4\pi M_0} \frac{1}{t_{\mathrm{FM}}}, \tag{A1}$$

where the first component α_0 is the intrinsic contribution and the second component is the additional damping due to spin pumping. Here, γ, M_0, $g_{\mathrm{eff}}^{\uparrow\downarrow}$ and t_{FM} are the gyromagnetic ratio, equilibrium magnetisation, effective spin-mixing conductance, and the thickness of the ferromagnetic layer. It is evident that the Gilbert damping parameter depends on the thickness of the ferromagnetic film in two ways: directly through the $1/t_{\mathrm{FM}}$ factor, and indirectly through the dependence on magnetisation. The latter dependence is especially important for very thin films in which the magnetisation decreases dramatically.

Magnetisation of thin films can be extracted from the FMR position, which is measured either from the microwave absorption or the induced voltage signal. For in-plane magnetic fields, the Kittel equation [47] describing the FMR condition takes the form

$$\left(\frac{\omega}{\gamma}\right)^2 = H_{\mathrm{FMR}}(H_{\mathrm{FMR}} + 4\pi M_0), \tag{A2}$$

and can be transformed to obtain M_0 given H_{FMR} and the microwave frequency ω. However, modelling magnetisation as a function of the ferromagnetic layer thickness is difficult, especially for an alloy such as Py which forms a multi-domain structure. Therefore, we use empirical modelling described below.

The plot of the extracted magnetisation vs. thickness of the ferromagnetic layer for Au/Py and Pt/Py bilayers is shown in fig. A1(a). It can be seen that M_0 does not change with thickness for thicker films but decreases rapidly for very thin films on the order of 10nm. We propose to model this trend with an equation based on a modified power law

$$M_0(t_{\mathrm{FM}}) = A - B t_{\mathrm{FM}}^{-\mathrm{n}}, \tag{A3}$$

where A,B and n are fitting parameters. Although such an empirical equation does not relate to a particular physical model, it provides an empirical, functional form

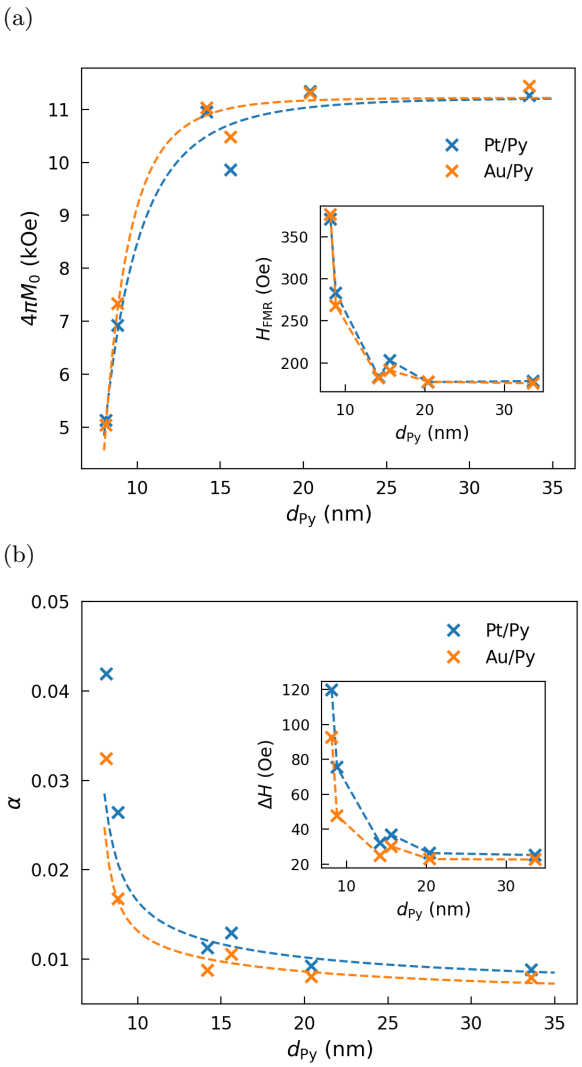

FIG. A1: Py thickness dependence of (a) the saturation magnetisation and (b) the Gilbert damping constant for two types of vertical bilayers with Pt (blue markers) and Au (orange markers) as the non-magnetic layer. Dashed lines show the numerical fits to the data.

to model magnetisation as a function of ferromagnetic film thickness, which is sufficient for the purpose of our experiments. The dashed lines in fig. A1(a) are the resulting fits to the data – they demonstrate that this simple relation can model the magnetisation in the range of Py film thickness used in our experiments.

Figure A1(b) shows the values of the Gilbert damping parameter extracted from the FMR linewidth using the relation $\alpha = \Delta H \cdot \gamma/\omega$ [33]. Using eq. A1 together with the functional form of M_0 extracted from fig. A1(a), we produced numerical fits of the data (dashed lines in fig. A1(b)) where α_0 and $g_{\text{eff}}^{\uparrow\downarrow}$ were treated as fitting parameters. We can see that α increases sharply for thin Py films, which is qualitatively consistent with eq. A1. However, the measured values for the thinnest films (8 nm) are significantly bigger than the numerical predictions. The parameters extracted in the process of numerical fitting are $\alpha_0 = 6.3 \times 10^{-3}$, $g_{\text{eff}}^{\uparrow\downarrow} = 4.63 \times 10^{15}$ cm^{-1} for Pt/Py and $\alpha_0 = 5.5 \times 10^{-3}$, $g_{\text{eff}}^{\uparrow\downarrow} = 3.79 \times 10^{15}$ cm^{-1} for Au/Py bilayers. While α_0 in both cases is comparable to the literature values [45], the effective spin-mixing conductance values are a few times bigger than previously reported. Consequently, the Gilbert damping constant of around 0.04 measured for 8 nm thick Py films is a few times bigger than reported in literature [45]. These discrepancies are suggestive of an extra broadening mechanism that increases damping in our experiments. It is likely to be caused by a non-uniform growth of the film at such small thickness values which results in a rough surface and influences the formation of magnetic domains.

The above modelling of the Gilbert damping constant using eq. A1 captures the general trend, however, it does not take into account the non-uniform growth of the ferromagnetic film, hence failing for very thin films. While the full modelling is beyond the scope of this paper, we note that this simple model fits the data reasonably well and therefore can be used to improve the numerical fits of Py thickness dependence of the voltage signal reported in the main text.

Appendix B

Figure A2 shows a schematic diagram of electrical connections in the setup used for lateral and vertical spin pumping measurements. It illustrates connections between the microwave generator (Anritsu MG396), lock-in amplifier (Stanford Research Systems SR860 DSP) used to control the field modulation coils and measure absorption signal, nanovoltmeter (Keithley 2182A) used to measure a DC voltage signal across the device, power supply for the electromagnet (KEPCO BOP), gaussmeter (LakeShore 455) and a rotating stage.

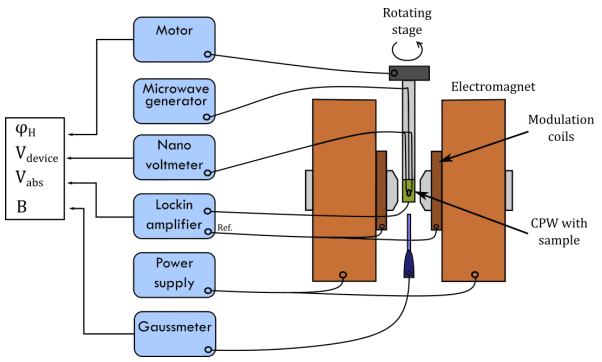

FIG. A2: A schematic diagram of electrical wiring in the experimental setup illustrating connections between different units which are used to measure the in-plane angle ϕ_H, device voltage V_{device}, microwave absorption signal V_{abs} and the magnetic field B.

[1] S. Schott, E. R. McNellis, C. B. Nielsen, H. Y. Chen, S. Watanabe, H. Tanaka, I. McCulloch, K. Takimiya, J. Sinova, and H. Sirringhaus, Tuning the effective spin-orbit coupling in molecular semiconductors., Nature Communications **8**, 15200 (2017).

[2] S. Schott, U. Chopra, V. Lemaur, A. Melnyk, Y. Olivier, R. D. Pietro, I. Romanov, R. L. Carey, X. Jiao, C. Jellett, M. Little, A. Marks, C. R. McNeill, I. McCulloch, E. R. McNellis, D. Andrienko, D. Beljonne, J. Sinova, and H. Sirringhaus, Polaron spin dynamics in high-mobility polymeric semiconductors, Nature Physics **15**, 814 (2019).

[3] Z. H. Xiong, D. Wu, Z. V. Vardeny, and J. Shi, Giant magnetoresistance in organic spin-valves, Nature **427**, 821 (2004).

[4] T. D. Nguyen, G. Hukic-Markosian, F. Wang, L. Wojcik, X. G. Li, E. Ehrenfreund, and Z. V. Vardeny, Isotope effect in spin response of pi-conjugated polymer films and devices., Nature Materials **9**, 345 (2010).

[5] T. D. Nguyen, E. Ehrenfreund, and Z. V. Vardeny, Spin-polarized light-emitting diode based on an organic bipolar spin valve, Science **337**, 204 (2012).

[6] S. Mooser, J. F. K. Cooper, K. K. Banger, J. Wunderlich, and H. Sirringhaus, Spin injection and transport in a solution-processed organic semiconductor at room temperature, Physical Review B **85**, 235202 (2012).

[7] F. Li, T. Li, F. Chen, and F. Zhang, Excellent spin transport in spin valves based on the conjugated polymer with high carrier mobility., Scientific Reports **5**, 9355 (2015).

[8] X. Zhang, S. Mizukami, T. Kubota, Q. Ma, M. Oogane, H. Naganuma, Y. Ando, and T. Miyazaki, Observation of a large spin-dependent transport length in organic spin valves at room temperature, Nature Communications **4**, 1392 (2013).

[9] S. Majumdar and H. S. Majumdar, On the origin of decay of spin current with temperature in organic spintronic devices, Organic Electronics **13**, 2653 (2012).

[10] N. A. Morley, A. Rao, D. Dhandapani, M. R. J. Gibbs, M. Grell, and T. Richardson, Room temperature organic spintronics, Journal of Applied Physics **103**, 07F306 (2008).

[11] Z.-G. Yu, Suppression of the hanle effect in organic spintronic devices, Bulletin of the American Physical Society **111**, 016601 (2014).

[12] Z. G. Yu, Spin-orbit coupling, spin relaxation, and spin diffusion in organic solids., Physical Review Letters **106**, 106602 (2011).

[13] Z. G. Yu, Impurity-band transport in organic spin valves, Nature Communications **5**, 4842 (2014).

[14] M. Grunewald, M. Wahler, F. Schumann, M. Michelfeit, C. Gould, R. Schmidt, F. Wurthner, G. Schmidt, and L. W. Molenkamp, Tunneling anisotropic magnetoresistance in organic spin valves, Physical Review B **84**, 125208 (2011).

[15] M. Grunewald, R. Gockeritz, N. Homonnay, F. Wurthner, L. W. Molenkamp, and G. Schmidt, Vertical organic spin valves in perpendicular magnetic fields, Physical Review B **88**, 085319 (2013).

[16] R. Göckeritz, N. Homonnay, A. Müller, B. Fuhrmann, and G. Schmidt, Resistive switching and voltage induced modulation of tunneling magnetoresistance in nanosized perpendicular organic spin valves, AIP Advances **6**, 45003 (2016).

[17] S. J. Wang, D. Venkateshvaran, M. R. Mahani, U. Chopra, E. R. McNellis, R. D. Pietro, S. Schott, A. Wittmann, G. Schweicher, M. Cubukcu, K. Kang, R. Carey, T. J. Wagner, J. N. Siebrecht, D. P. Wong, I. E. Jacobs, R. O. Aboljadayel, A. Ionescu, S. A. Egorov, S. Mueller, O. Zadvorna, P. Skalski, C. Jellett, M. Little, A. Marks, I. McCulloch, J. Wunderlich, J. Sinova, and H. Sirringhaus, Long spin diffusion lengths in doped conjugated polymers due to enhanced exchange coupling, Nature Electronics **2**, 98 (2019).

[18] R. H. Silsbee, A. Janossy, and P. Monod, Coupling between ferromagnetic and conduction-spin-resonance modes at a ferromagnetic-normal-metal interface, Physical Review B **19**, 4382 (1979).

[19] Y. Tserkovnyak, A. Brataas, and G. E. W. Bauer, Enhanced gilbert damping in thin ferromagnetic films., Physical Review Letters **88**, 117601 (2002).

[20] E. Saitoh, M. Ueda, H. Miyajima, and G. Tatara, Conversion of spin current into charge current at room temperature: Inverse spin-hall effect, Applied Physics Letters **88**, 182509 (2006).

[21] J. Sinova, S. O. Valenzuela, J. Wunderlich, C. H. Back, and T. Jungwirth, Spin hall effects, Reviews of Modern Physics **87**, 1213 (2015).

[22] R. Iguchi and E. Saitoh, Measurement of spin pumping voltage separated from extrinsic microwave effects, Journal of the Physical Society of Japan **86**, 11003 (2017).

[23] E. Shikoh, K. Ando, K. Kubo, E. Saitoh, T. Shinjo, and M. Shiraishi, Spin-pump-induced spin transport in p-type si at room temperature., Physical Review Letters **110**, 127201 (2013).

[24] A. Yamamoto, Y. Ando, T. Shinjo, T. Uemura, and M. Shiraishi, Spin transport and spin conversion in compound semiconductor with non-negligible spin-orbit interaction, Physical Review B **91**, 024417 (2015).

[25] Z. Tang, E. Shikoh, H. Ago, K. Kawahara, Y. Ando, T. Shinjo, and M. Shiraishi, Dynamically generated pure spin current in single-layer graphene, Physical Review B **87**, 140401(R) (2013).

[26] S. Dushenko, M. Koike, Y. Ando, T. Shinjo, M. Myronov, and M. Shiraishi, Experimental demonstration of room-temperature spin transport in n-type germanium epilayers., Physical Review Letters **114**, 196602 (2015).

[27] T. Yamamoto, T. Seki, S. Ono, and K. Takanashi, Characterization of spin pumping effect in permalloy/cu/pt microfabricated lateral devices, Journal of Applied Physics **115**, 17C505 (2014).

[28] R. Ohshima, Y. Ando, K. Matsuzaki, T. Susaki, M. Weiler, S. Klingler, H. Huebl, E. Shikoh, T. Shinjo, S. T. B. Goennenwein, and M. Shiraishi, Strong evidence for d-electron spin transport at room temperature at a laalo3/srtio3 interface., Nature Materials **16**, 609 (2017).

[29] L. Bai, Z. Feng, P. Hyde, H. F. Ding, and C.-M. Hu, Distinguishing spin pumping from spin rectification in a pt/py bilayer through angle dependent line shape analysis, Applied Physics Letters **102**, 242402 (2013).

[30] L. Bai, P. Hyde, Y. S. Gui, C. M. Hu, V. Vlaminck, J. E. Pearson, S. D. Bader, and A. F. Hoffmann, Universal method for separating spin pumping from spin rectifica-

tion voltage of ferromagnetic resonance., Physical Review Letters **111**, 217602 (2013).

[31] M. Harder, Z. X. Cao, Y. S. Gui, X. L. Fan, and C.-M. Hu, Analysis of the line shape of electrically detected ferromagnetic resonance, Physical Review B **84**, 054423 (2011).

[32] W. T. Soh, B. Peng, and C. K. Ong, An angular analysis to separate spin pumping-induced inverse spin hall effect from spin rectification in a py/pt bilayer, Journal of Physics D **47**, 285001 (2014).

[33] T. Gilbert, A phenomenological theory of damping in ferromagnetic materials, IEEE Transactions on Magnetics **40**, 3443 (2004).

[34] K. Ando, S. Takahashi, J. Ieda, Y. Kajiwara, H. Nakayama, T. Yoshino, K. Harii, Y. Fujikawa, M. Matsuo, S. Maekawa, and E. Saitoh, Inverse spin-hall effect induced by spin pumping in metallic system, Journal of Applied Physics **109**, 103913 (2011).

[35] H. J. Juretschke, Electromagnetic theory of dc effects in ferromagnetic resonance, Journal of Applied Physics **31**, 1401 (1960).

[36] B. F. Miao, S. Y. Huang, D. Qu, and C. L. Chien, Inverse spin hall effect in a ferromagnetic metal, Phys. Rev. Lett. **111**, 066602 (2013).

[37] A. Tsukahara, Y. Ando, Y. Kitamura, H. Emoto, E. Shikoh, M. P. Delmo, T. Shinjo, and M. Shiraishi, Self-induced inverse spin hall effect in permalloy at room temperature, Phys. Rev. B **89**, 235317 (2014).

[38] H. Liu, C. Zhang, H. Malissa, M. Groesbeck, M. Kavand, R. McLaughlin, S. Jamali, J. Hao, D. Sun, R. A. Davidson, L. Wojcik, J. S. Miller, C. Boehme, and Z. V. Vardeny, Organic-based magnon spintronics, Nature Materials **17**, 308 (2018).

[39] H. Liu, H. Malissa, R. M. Stolley, J. Singh, M. Groesbeck, H. Popli, M. Kavand, S. K. Chong, V. V. Deshpande, J. S. Miller, C. Boehme, and Z. V. Vardeny, Spin wave excitation, detection, and utilization in the organic-based magnet, v(tcne)x (tcne = tetracyanoethylene), Advanced Materials **32**, 2002663 (2020).

[40] S. A. Manuilov, C. H. Du, R. Adur, H. L. Wang, V. P. Bhallamudi, F. Y. Yang, and P. C. Hammel, Spin pumping from spinwaves in thin film yig, Applied Physics Letters **107**, 42405 (2015).

[41] X. Tao, Q. Liu, B. Miao, R. Yu, Z. Feng, L. Sun, B. You, J. Du, K. Chen, S. Zhang, L. Zhang, Z. Yuan, D. Wu, and H. Ding, Self-consistent determination of spin hall angle and spin diffusion length in pt and pd: The role of the interface spin loss, Science Advances **4**, eaat1670 (2018).

[42] K. Roy, Estimating the spin diffusion length and the spin hall angle from spin pumping induced inverse spin hall voltages, Physical Review B **96**, 174432 (2017).

[43] W. Zhang, V. Vlaminck, J. E. Pearson, R. Divan, S. D. Bader, and A. Hoffmann, Determination of the pt spin diffusion length by spin-pumping and spin hall effect, Applied Physics Letters **103**, 242414 (2013).

[44] M. Isasa, E. Villamor, L. E. Hueso, M. Gradhand, and F. Casanova, Temperature dependence of spin diffusion length and spin hall angle in au and pt, Physical Review B **91**, 024402 (2015).

[45] A. Azevedo, L. H. Vilela-Leao, R. L. Rodriguez-Suarez, A. F. L. Santos, and S. M. Rezende, Spin pumping and anisotropic magnetoresistance voltages in magnetic bilayers: Theory and experiment, Physical Review B **83**, 144402 (2011).

[46] S. Watanabe, K. Ando, K. Kang, S. Mooser, Y. Vaynzof, H. Kurebayashi, E. Saitoh, and H. Sirringhaus, Polaron spin current transport in organic semiconductors, Nature Physics **10**, 308 (2014).

[47] C. Kittel, On the theory of ferromagnetic resonance absorption, Physical Review D **73**, 155 (1948).